Pore-lean directed energy deposition additive manufacturing through laser power modulation

Kai Zhang, Shishira Bhagavath, Sebastian Marussi, Alexander Rack, Robert Atwood, Martyn A. Jones, Chu Lun Alex Leung, Chinnapat Panwisawas, Junji Shinjo, Peter D. Lee

PII: \$1359-6454(25)00801-8

DOI: https://doi.org/10.1016/j.actamat.2025.121515

Reference: AM 121515

To appear in: Acta Materialia

Received date: 2 July 2025

Revised date: 1 September 2025 Accepted date: 5 September 2025



Please cite this article as: Kai Zhang, Shishira Bhagavath, Sebastian Marussi, Alexander Rack, Robert Atwood, Martyn A. Jones, Chu Lun Alex Leung, Chinnapat Panwisawas, Junji Shinjo, Peter D. Lee, Pore-lean directed energy deposition additive manufacturing through laser power modulation, *Acta Materialia* (2025), doi: https://doi.org/10.1016/j.actamat.2025.121515

This is a PDF file of an article that has undergone enhancements after acceptance, such as the addition of a cover page and metadata, and formatting for readability, but it is not yet the definitive version of record. This version will undergo additional copyediting, typesetting and review before it is published in its final form, but we are providing this version to give early visibility of the article. Please note that, during the production process, errors may be discovered which could affect the content, and all legal disclaimers that apply to the journal pertain.

© 2025 Published by Elsevier Inc. on behalf of Acta Materialia Inc.

Pore-lean directed energy deposition additive manufacturing through laser power modulation

Kai Zhang ^{1,2,3,4,*}, Shishira Bhagavath ^{1,4}, Sebastian Marussi ^{1,4}, Alexander Rack ⁵, Robert Atwood ⁶, Martyn A. Jones ⁷, Chu Lun Alex Leung ^{1,3}, Chinnapat Panwisawas ⁸, Junji Shinjo ⁹, Peter D. Lee^{1,4,*}

Abstract

Directed energy deposition (DED) laser additive manufacturing (AM) is a promising technique for building complex components and performing repair applications. However, large defects can form through coalescence of argon bubbles from the feedstock powder, potentially reducing end-component mechanical performance. Here, we used correlative high-speed synchrotron X-ray and infrared imaging, coupled with multiphysics modelling to develop a strategy to control defect formation. We demonstrate that the bubble dynamics can be controlled by appropriately modulating the laser power, temporarily disrupting the Marangoni flow, enabling bubble release. The bubble control mechanisms discovered here provide a way to achieve defect-lean AM.

Keywords: Additive manufacturing; Porosity; Laser deposition; X-ray synchrotron radiation; Modelling.

1

¹ Mechanical Engineering, University College London, London, WC1E 7JE, UK

² School of Electrical, Electronic and Mechanical Engineering, University of Bristol, Bristol, BS8 1TR, UK

³ Faculty of Science and Engineering, Swansea University, Bay Campus, Swansea, SA1 8EN, UK

⁴ Research Complex at Harwell, Harwell Campus, Didcot, OX11 0FA, UK

⁵ ESRF - The European Synchrotron, Grenoble, 38000, France

⁶ Diamond Light Source, Harwell Campus, Oxfordshire, OX11 0DE, UK

⁷ Rolls-Royce plc, PO Box 31, Derby, DE24 8BJ, UK

⁸ School of Engineering and Materials Science, Queen Mary University of London, London, E1 4NS, UK

⁹ Next Generation Tatara Co-Creation Centre, Shimane University, Matsue, 690-8504, Japan

^{*} Corresponding authors: <u>kai-zhang@ucl.ac.uk</u>; <u>peter.lee@ucl.ac.uk</u>

1. Introduction

Directed energy deposition (DED) is a promising additive manufacturing (AM) technology enabling layer-by-layer fabrication of complex components, attracting significant interest from aerospace, automotive and other industries [1–4]. However, DED-AM components may contain defects, *e.g.* porosity and cracks [5–8], which deteriorate their mechanical performance and limit their applications [9,10]. Therefore, it is critical to develop novel strategies to minimise porosity.

Several pore formation mechanisms occur during AM including hydrogen porosity [11], pores originating from powder feedstocks [5], keyhole collapse [12–14] and particle impact [15]. High-speed synchrotron X-ray imaging is an ideal *in situ* tool to reveal and quantify bubble behaviour and melt flow during AM processes [5,13,16–23]. In laser powder bed fusion (LPBF), keyhole morphology and dynamics were revealed with high-energy X-rays, demonstrating their dependency on laser power, power density and scan velocity [18]. However, the bubble formation and elimination mechanisms in the DED process still need further investigation.

One of the main sources of porosity in DED originates from trapped argon bubbles in the gas atomised powder feedstock, which are then transferred into the melt, coalesce, and form large pores [5]. These large bubbles are retained in the melt pool by the very high shear from the Marangoni surface flow. Pores in DED have also been observed to form by either unstable keyhole dynamics or entrainment of

shielding gas behind powder particles entering the molten pool [17]. However, this study used a laser with a small beam diameter operated in keyhole mode [17] while most industrial DED machines operate in conduction mode, hence keyhole pores are not expected. These prior *in situ* studies [5,17] did not propose strategies to control or minimise porosity.

Strategies for laser beam power oscillation have been applied to alter the microstructure, improving grain refinement in Ti6Al4V via inducing a columnar-to-equiaxed transition, enhancing its strength and elongation [24]. Another strategy tested for welding was applying a pulsed magnetic field to increase precipitate density and tensile strength in aluminium alloys [25]. In LPBF, pulsing the laser power was found to cause keyhole collapse resulting in occasional pore formation [26], and enhance strength in CrCoNi alloy [27]. However, the impact of different laser modulation strategies in DED is still uncertain.

In this work, we hypothesise that disrupting the Marangoni surface flow might allow coalescing bubbles to escape. By reducing the laser heat flux for a short time, the surface thermal gradient will be reduced, reducing Marangoni flow, allowing buoyancy to remove bubbles before they become large. Here we test different laser modulation strategies, including sinusoidal and pulsed waves at different frequencies, to control and minimise bubbles. We quantify the underlying mechanisms and efficacy using correlative *in situ* high-speed synchrotron X-ray and infrared (IR)

imaging, coupled with multiphysics modelling to validate the underlying phenomena. We determine the laser power modulation waveform (sinusoidal or pulsed wave), frequency and duration time required to prevent large bubble formation, resulting in pore-lean AM builds, confirming the underlying mechanisms via high fidelity multiphysics modelling.

2. Methods

2.1. Materials

The gas-atomised powder is high gamma prime nickel-based superalloy RR1000 which was provided by Rolls-Royce plc. The powder particle distribution is 53-106 µm with a D50 size of ~73 µm. In some experiments 4 wt.% tungsten (W) flow-tracer particles are mixed with these powders to track the flow patterns. The corresponding powder size distribution and morphology are shown in **Fig. S1**.

2.2. High-speed synchrotron X-ray imaging

The *in situ* high-speed synchrotron X-ray imaging experiments were conducted in an ID19 beamline at the European Synchrotron Radiation Facility (ESRF). The correlative X-ray imaging and infrared imaging were conducted in beamline I12 at Diamond Light Source (DLS). The high-speed X-ray imaging experiments at ESRF were performed with a CMOS camera (type: SAZ, Photron, Japan) lens-coupled to a LuAG:Ce single-crystal scintillator at a frame rate of 20 kHz, a spatial resolution of ~4 µm/pixel. The longer, but lower speed, X-ray imaging

experiments at DLS were performed using a MIRO310M detector with optical module 3 and a LuAg:Ce scintillator at a frame rate of 1 kHz, a spatial resolution of \sim 6.67 μ m/pixel.

2.3. Blown Powder Additive Manufacturing Process Replicator II system

The Blown Powder Additive Manufacturing Process Replicator II (BAMPR II) is designed to simulate the directed energy deposition additive manufacturing process and integrate with the beamline for in situ synchrotron X-ray experiments. BAMPR II is equipped with a 500 W TruFiber laser to achieve both continuous and modulated modes. We mainly apply two typical laser modulations including sinusoidal waveform (SW) and pulsed waveform (PW) modes in this work. The OPTOGAMA beam reducer is aligned well with the laser beam to achieve a selectable beam diameter of 100-700 µm. The 4-hole nozzle coaxial head is aligned with the laser beam and beam reducer, and powder originates from the powder feeder and through the pipeline with argon gas, and spreads out from the nozzle. The 3-axis moving stage can move in 3 directions with a speed range of 0.5 - 50 mm s⁻¹. The substrate is clamped with the sample stage, so the laser can melt the powder over the substrate. The oxygen level in the environmental chamber is controlled to be below 100 ppm during the additive manufacturing process. To compare between modulated mode and continuous mode, the mean laser powers calculated in each period were kept the same.

2.4. Thermal imaging

The thermal imaging was performed simultaneously with X-ray imaging to achieve correlative observation. The thermal imaging camera is FLIR X6900sc (FLIR Systems, Inc., USA). The camera is set up with a macro lens with a pixel size of 32.7 µm. The frame rate in this work is 1 kHz. The IR camera was calibrated at the FLIR camera company using numerous blackbody reference sources under controlled conditions. The blackbody reference sources were set to different known temperatures, and the camera was sequentially aligned with each reference source. The signal value at each temperature is captured by calibration software, and the corresponding signal and temperature values are used to construct a calibration curve. The data is subsequently uploaded to the camera, calibrating it to ensure compliance with accuracy specifications. The temperature is corrected with an emissivity value of 0.25 based on the measured experimental data [28]. This thermal image of the pool surface was taken at 40° from horizontal.

2.5. Material characterisation

Electron backscatter diffraction (EBSD, AZtec Oxford Instruments) analysis was conducted to analyse the grain size and morphology of the DED-AM builds. The electron beam is 20 kV and the step size is 5 μ m. The computational tomography (CT) was conducted to analyse the porosity of the AM builds with a Nikon XT H 225 micro-CT with an effective voxel size of ~4.5 μ m and a beam voltage of 149 kV, and

the CT datasets were reconstructed with the CT Pro 3D software. The *ex situ* X-ray radiographs of the AM builds were performed using a GE Phoenix v|tome|x 160 lab XMT machine with an average pixel size of ~6.5 μm.

2.6. Image processing

The acquired radiographs were conducted with flat correction by raw images divided by the average of 100 images. The trajectories of bubbles and W particles (flow) were tracked by the ImageJ Plugin TrackMate [29]. To present the thermal imaging information as a function of time and frequency, wavelet analysis was conducted to transform the time-series data to the wavelet scalogram with a continuous wavelet transform function in MATLAB.

2.7. Multi-physics modelling

High-fidelity multi-physics modelling based on computational fluid dynamics (CFD) was used to elucidate the temperature and Marangoni flow fields under laser power modulation. The method includes molten fluid flow, phase change, liquid/solid/gas interface tracking, heat transfer, surface tension (with the Marangoni effect) and laser ray tracing.

The modelling analysis was based on the computational fluid dynamics (CFD) methodology [30,31]. The fluid flow equations of mass, momentum and temperature were solved in a fully coupled way, which are given as

$$\frac{\partial \rho}{\partial t} + (\boldsymbol{u} \cdot \boldsymbol{\nabla})\rho = -\rho \boldsymbol{\nabla} \cdot \boldsymbol{u}$$

(1)

$$\frac{\partial u}{\partial t} + (u \cdot \nabla)u = -\frac{\nabla p}{\rho} + Q_u + g + \frac{1}{\rho} F_{u,surf}$$

(2)

$$\frac{\partial T}{\partial t} + (\boldsymbol{u} \cdot \nabla)T = -\frac{p\nabla \cdot \boldsymbol{u}}{\rho c_p} + Q_T$$

(3)

where ρ is the density, \boldsymbol{u} is the velocity, T is the temperature, p is the pressure and c_p is the constant-pressure heat capacity. $\boldsymbol{Q}_{\mathbf{u}}$ represents the Newtonian viscous force and Darcy's force in the mushy zone, given by

$$Q_{u,i} = \frac{1}{\rho} \frac{\partial \tau_{ij}}{\partial x_j} - \frac{\nu}{\kappa} \left(\frac{(1 - f_L)^2}{f_L^3} \right) u_i, \quad \tau_{ij} = \mu \left(\frac{\partial u_i}{\partial x_j} + \frac{\partial u_j}{\partial x_i} \right) - \frac{2}{3} \mu \nabla \cdot \boldsymbol{u} \delta_{ij}$$

$$(4)$$

where K is the permeability coefficient related to the grain scale, f_L is the liquid fraction determined by the temperature, ν is the kinematic viscosity and μ is the dynamic viscosity. g is the gravitational acceleration. $F_{u,surf}$ represents the interfacial surface tension force with the Marangoni effect, formulated as

$$\mathbf{F}_{u,surf} = \sigma \kappa \delta \mathbf{n} + (\nabla \sigma - (\nabla \sigma \cdot \mathbf{n}) \mathbf{n}) \delta \tag{5}$$

where $\sigma = \sigma(T)$ is the temperature-dependent surface tension coefficient, κ is the local surface curvature and \mathbf{n} is the unit vector normal to the surface. δ is a surface identifier which is non-zero only on the surface. Q_T represents the heat transport, including heat conduction by Fourier's law, viscous work, latent heat for phase

change and radiation, given as

$$Q_{T} = \frac{1}{\rho c_{p}} \left[\nabla \cdot (\lambda \nabla T) + \frac{\partial \tau_{ij} u_{i}}{\partial x_{j}} - \frac{D \rho \Delta h}{D t} \right] + \varepsilon \sigma_{SB} (T^{4} - T_{0}^{4}) |\nabla \varphi|$$
(6)

where Δh is the latent heat. φ ($0 \le \varphi \le 1$) is a colour function to identify the surface. Radiation is included on the heated metal surface identified by the gradient of $|\nabla \varphi|$, with σ_{SB} the Stefan-Boltzmann constant and ε the emissivity. The laser power is given to the melt pool surface by the ray tracing method and the absorbed heat is given on the surface as a source term. The laser power is given by the Gaussian profile and its power is modulated according to the control scheme. The physical properties such as viscosity and thermal conductivity are retrieved from the reference [30,31].

The free surface was captured by the combined Level-Set/Volume-Of-Fluid (CLSVOF) method to assure shape accuracy and volume conservation. The level-set function (signed distance function from the surface) is governed by

$$\frac{\partial F}{\partial t} + (\boldsymbol{u} \cdot \boldsymbol{\nabla})F = |\nabla F| \frac{dN}{dt}$$

(7)

where dN/dt is the surface growth speed due to metal deposition and is estimated from the powder feeding rate. The colour function φ is a heaviside function of F and the density at the melt pool surface, for example, is given by $\rho = (1 - \varphi)\rho_G + \varphi \rho_L$ where ρ_L and ρ_G are the liquid and gas density, respectively. The bubbles inside the melt pool are not directly tracked for the cases in which the main objective is to show

the temperature and Marangoni flow field variation due to the laser modulation, and tracked both in a directly resolved way or as point-particles for the cases to investigate the bubble motions.

The numerical scheme was based on a CIP (Constrained Interpolation Profile) method, in which a third-order polynomial fitting is used for flow variables and their derivatives to assure the accuracy. Further details of the numerical method can be found in [30,31]. Here, the grid resolution is set as 32 µm, which is the same as in the previous analysis [5]. This resolution is for simulating the longer time behaviour and sensitivity studies illustrated that this resolution can reproduce the temperature and Marangoni flow structures in the melt pool for the present experimental setup. For the resolved bubble tracking cases, a finer grid resolution of 16 µm is used.

3. Results and discussion

3.1. Pore formation mechanisms during DED using a continuous wave laser

During DED, the bubble behaviour includes bubble formation, circulation, coalescence, motion, entrainment, escape and entrapment. These phenomena were captured using synchrotron high-speed X-ray imaging in a second generation *in situ* DED rig equipped with a modulated laser system (BAMPR-II [5], see Fig. S2) at the European Synchrotron (ESRF France) and Diamond Light Source (UK) (see Methods). Fig. 1a shows how small argon gas pores entrapped in the powder

feedstock are released into the melt pool when the powder particles enter the melt pool (blue dashed circles). These small argon bubbles, recirculate outward at the front and rear of the melt pool, driven by the Marangoni flow. Some of the small argon bubbles coalesce to form large bubbles (see **Fig. 1b** and Movie S1), while some are entrapped by the solidification front and others escape from the pool's surface. The large bubbles remain entrained in the molten pool and continue growing (**Fig. 1c**), forced down by the high Marangoni surface shear flow (see **Fig. 1d,e**). The growth of these large bubbles via coalescence of small ones was quantitatively analysed (see **Fig. 1f**). The bubbles show a periodic growth trend, reaching a critical size of approx. 80 µm (under the conditions studied) after which they escape from the melt pool surface. Occasionally, some of these large pores are entrapped by the solidification front, especially, at the end of track when the laser is powered off.

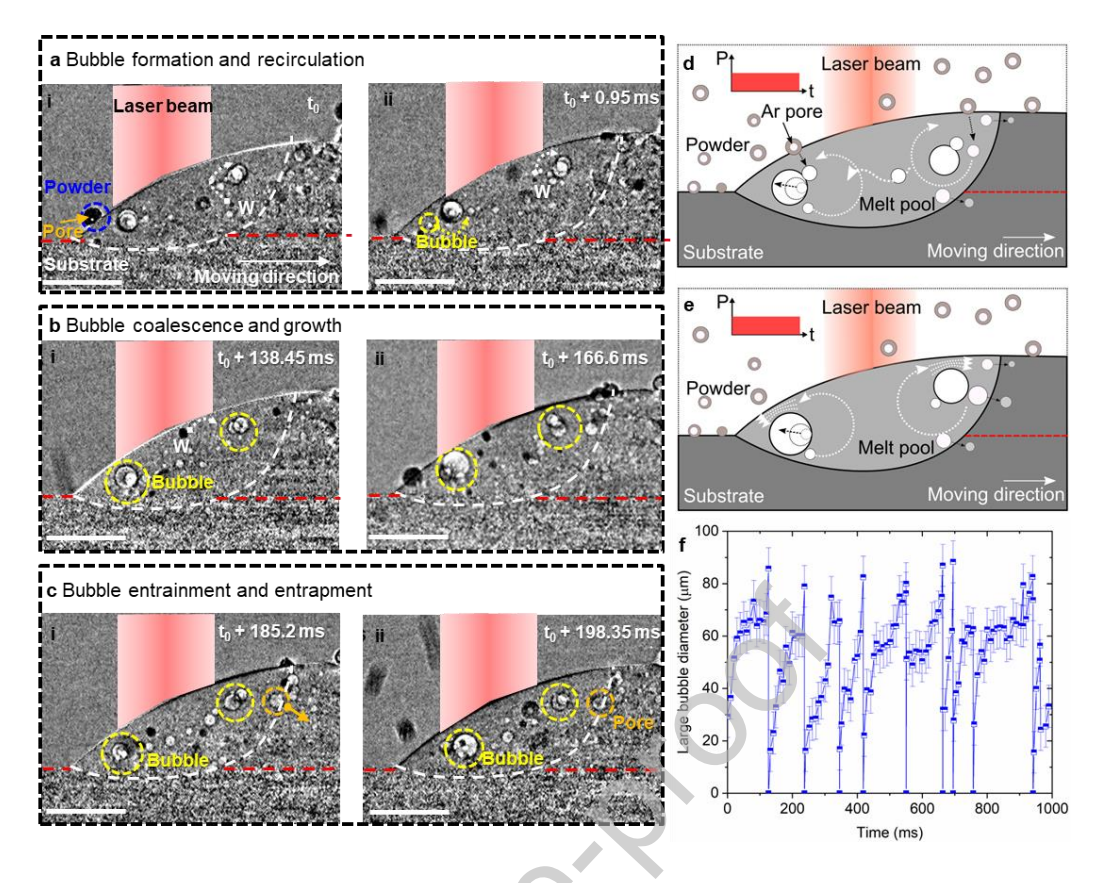


Fig. 1 Bubble behaviour during DED in continuous wave (CW) mode. (a)-i An argon pore in a powder forming a small bubble in the melt (blue dashed circle) at $t = t_0$; (a)-ii the formed bubble recirculation and W tracer (black) motion are indicated by yellow and white dashed arrows, respectively, at $t = t_0 + 0.95$ ms. (b) Radiographs showing the bubble coalescence (yellow dashed circles) and growth at (b)-i $t = t_0 + 138.45$ and (b)-ii $t_0 + 166.6$ ms; and W tracer motion (white dashed arrow). (c) Bubble entrainment and entrapment (orange dashed circles) at (c)-i $t = t_0 + 185.2$ and (c)-ii $t_0 + 198.35$ ms. (d) and (e), corresponding schematic figures of (a) and (b). (f) Large bubble diameter as a function of time, and diameter error bars are calculated as ± 2 pixels, equivalent to segmentation uncertainty. (Substrate traverse speed 1 mm s⁻¹, laser power 150 W, layer 1. See the corresponding video of (a to c) in Movie S1. Scale bars: 300 µm).

Fig. 1 demonstrates that the strong Marangoni shear flow enables the smaller argon bubbles to coalesce and grow to a large and potentially detrimental size, if entrapped by the solidification front. We hypothesise that the Marangoni flow can be

disrupted by an appropriate duration and type of laser power modulation, allowing the bubbles to escape. To test this hypothesis, we investigated a range of frequency modulations ranging from 5 to 500 Hz, for both sinusoidal waveform (SW) and pulsed waveform (PW).

3.2. Controlling bubbles using sinusoidal waveform (SW) modulated laser power

The bubble behaviour with laser modulation in sinusoidal mode has three main stages (see Fig. 2, Movie S2, mean power 150 W, SW 20 Hz): I. laser power ramping up to maximum - bubble entrainment from powder and recirculation allowing coalescence and large bubble growth; II. laser power ramping down decreasing Marangoni flow, reducing small bubble flow and hence coalescence; III. minimum laser power - minimising Marangoni flow, leading to buoyancy-driven bubble escape. Fig. 2a,d shows stage I, where bubbles transfer from the melting feedstock powder into the molten pool. These bubbles circulate in the front and back of the melt pool and are driven by the strong Marangoni flow at peak laser power (250 W). In stage II (Fig. 2b,e), the laser power decreases to a mean of 150 W, reducing the surface temperature gradient and hence Marangoni flow, reducing the flow velocity and hence coalescence of the small bubbles. In stage III (Fig. 2c,f), the laser power decreases further to the minimum (50 W) and the large bubble's buoyancy overcomes the weak Marangoni shear, and escapes out of the top of the melt pool. When in 20 Hz SW mode, there is insufficient time for significant bubble coalescence, hence no

bubble becomes larger than 29 ± 1 µm, and these bubbles are three times smaller than those formed under continuous wave (CW) mode where dozens of the small bubbles coalesce forming bubbles with a maximum size of 80 ± 3 µm (**Fig. 2h**, see Movie S3). As hypothesised, varying the laser power varies the Marangoni flow, both enabling pore release and limiting coalescence.

A range of SW frequency (5 to 500 Hz) DED builds were observed with synchrotron imaging and the maximum pore size quantified and compared to CW builds in **Fig. 2g,h**. The change in maximum bubble diameter versus duration time for the large bubble growth each cycle is plotted in **Fig. 2g**. For 20 Hz, the maximum bubble size remains relatively constant due to little bubble coalescence. At 5 Hz (**Fig. 2h**, Movie S3), the period of high laser power is ca. 100 ms, providing sufficient time for bubbles to coalesce, and as the peak power (250 W) is higher than the maximum for the CW mode (150 W), the peak pool size is larger, enabling a larger critical pore size (93 \pm 6 μ m). Our hypothesis breaks down if the frequency of modulation is too slow, as could be estimated from **Fig. 1f** where the duration time to reach the critical maximum size for CW can be seen to be less than 150 ms.

At the other extreme, 500 Hz SW, many pores recirculate without escaping, and some pore coalescence occurs, as shown in **Fig. 2g,h** (and Movie S4) with the maximum size reaching 43 ± 2 µm. Here, we hypothesise, that the time at which the laser power is at a minimum is so short (less than 1 ms) that the Marangoni flow does

not have time to reduce sufficiently in intensity, and the surface shear keeps coalescing pores from escaping, although at one half the maximum pore diameter of CW. Extreme high frequency SW (>1 kHz) effectively becomes CW mode laser operation, in terms of the surface temperature gradient and hence pool flow. In summary, for this mean laser power of 150 W, **Fig. 2g** shows that the optimum sinusoidal laser frequency modulation to prevent large pore coalescence is between 20 to 500 Hz (see Movies S2 and S4-6).

The influence of mean laser power (100-200 W) was also explored (**Fig. S3**) at a fixed pulse frequency of 20 Hz. Neither the maximum bubble diameter nor duration time changed as the mean laser power increased from 100 to 150 W (*ca.* 30 µm pore diameter and 20 ms duration). However, at 200 W mean power, significant bubble coalescence occurs, with the largest bubble diameter reaching 110 µm, and the duration 121 ms, significantly longer than for lower laser powers. At 200 W mean power, the instantaneous power ranges from 100-300 W; for this range of laser power, the pool always remains relatively large even during low power, reducing bubble escape. Therefore, the optimal mean laser power at 20 Hz would be below 150 W to achieve the minimal porosity.

The influence of multi-layer build was then investigated for the same conditions (SW mode, 20 Hz, 150 W, 1 mm s⁻¹) for up to 4 layers (summarised in **Fig. S4**). The maximum bubble diameter remains small (<50 µm) in all 4 layers. There is a

slight increase in maximum bubble diameter going from layer 1 to 2, thought to be due to more argon bubbles entering the pool from entrapped pores in the previous layers.

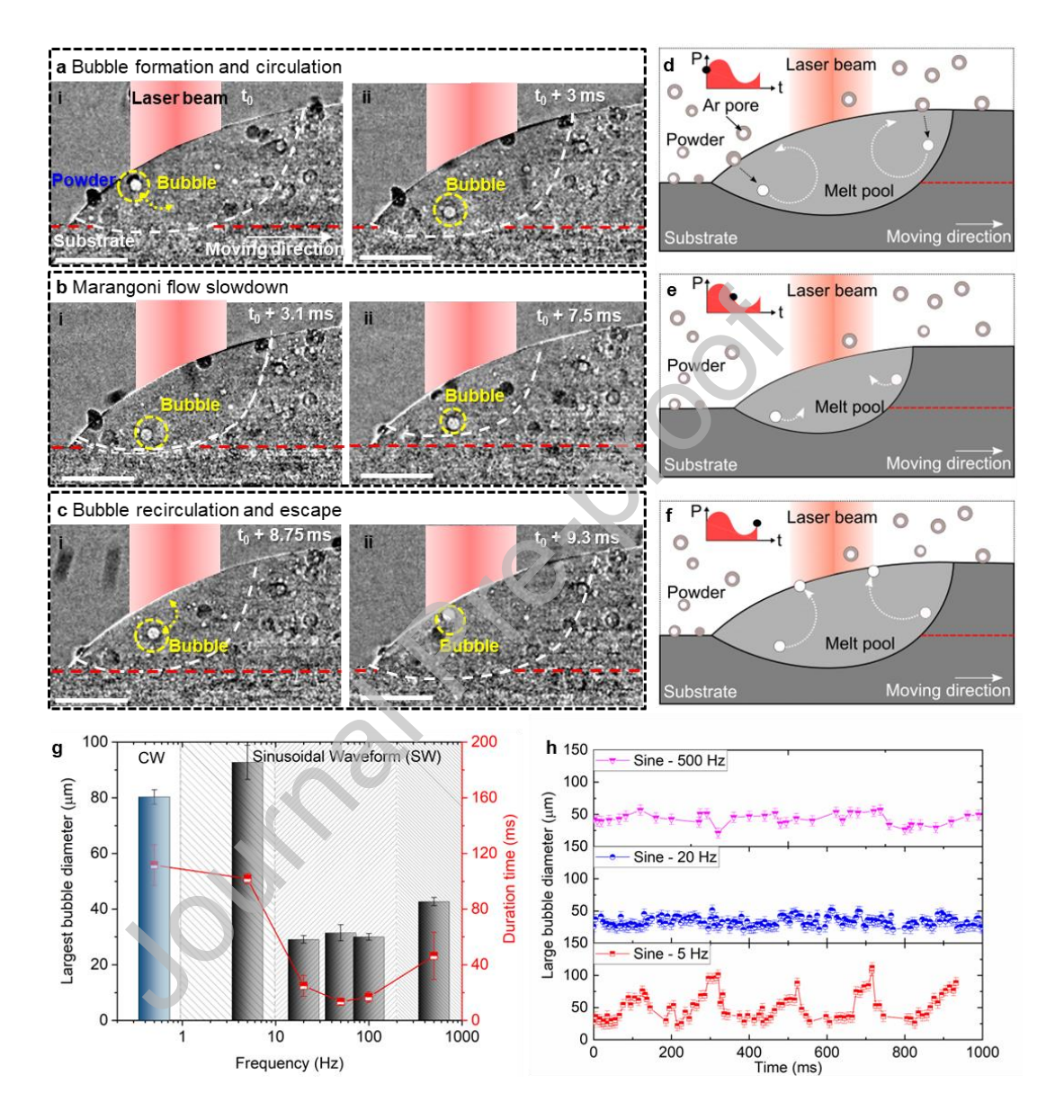


Fig. 2 Bubble behaviour and mechanisms during DED with a modulated laser in sinusoidal waveform (SW) mode. (a) Radiographs showing the bubble formation and circulation at (a)-i $t = t_0$ and (a)-ii $t_0 + 3$ ms. Bubble motion is indicated by the yellow dashed arrow. (b) Radiographs showing bubble slow down at (b)-i $t = t_0 + 3.1$ and (b)-ii $t_0 + 7.5$ ms. (c) Radiographs showing the bubble recirculation and escape at (c)-i $t = t_0 + 8.75$ and (c)-ii t_0

+ 9.3 ms at 20 Hz. (**d to f**) Corresponding schematics of (a to c). (**g**) Largest bubble diameter and duration time of bubble growth for CW and SW mode at frequencies from 5 to 500 Hz, and the error bar is standard error of the large bubble diameter and duration time in each cycle. (**h**) Largest bubble diameter evolution for SW mode at frequencies of 5, 20, and 500 Hz, and diameter error bars are calculated as ±2 pixels, equivalent to segmentation uncertainty. (The substrate traverse speed 1 mm s⁻¹, layer 1, mean and peak laser power is 150 and 250 W in SW mode and mean laser power of 150 W in CW, respectively. See corresponding videos to (a to c), (g) and (h) in Movies S2-6. Radiograph scale bars: 300 μm).

3.3. Controlling bubbles using pulsed waveform (PW) modulated laser power

The bubble behaviour with a modulated laser in a PW mode was investigated (see Fig. 3a-c). In Fig. 3a,d, the transfer of an argon bubble from a feedstock powder particle into the melt pool is captured. As the melt pool partially remelts the previously built track, pores in the prior track are released and form recirculating bubbles (see Fig. 3b). The melt pool expands and contracts as the laser is modulated from 0 to 300 W to achieve a 150 W mean power with a 50% duty cycle (DC), 20 Hz PW.

At peak power, the melt pool size grows to its largest extent, with bubbles recirculating and coalescing in both the front and rear of the melt pool (Fig. 3b,e). Unlike SW, where the peak power is reached for a short period, PW has 50 ms at 300 W, giving sufficient time for larger bubbles to form. In Fig. 3c,f, when the laser power reduces to 0, the melt pool shrinks quickly, entrapping both small and large bubbles in the build track (see Movie S7). However, at 50-500 Hz the time at full

power is sufficiently short to suppress coalescence, and the bubbles are released as the power reduces and Marangoni flow is suppressed, as summarised quantitatively in **Fig. 3g,h** for PW mode, and shown for 500 Hz in **Fig. S5**. Therefore, the optimal frequency range is smaller for PW mode, 50-500 Hz, as compared to 20-500 Hz for SW mode.

Bubble growth and coalescence at different DCs of 30%, 50% and 75% were investigated for 20 Hz PW and a mean power of 150 W (**Fig. S6** and Movie S7 for DC of 50%). The mean power of 150 W was maintained by changing the minimum and maximum powers (**Fig. S6c-e**). The largest bubble diameter decreases with increasing duty cycle from 30% to 75% (**Fig. S6**).

At 30% DC, a high maximum power (500 W) is on for 15 ms, creating a large pool, enabling lots of bubble coalescence. When the power goes off, the pool size shrinks quickly, entraining large bubbles in the solid, which are released in the next high-power cycle. Therefore, having a short duty cycle at high power is not appropriate for pore-lean production.

At 75% DC, the power is on for 37.5 ms, but at 200 W, with a smaller pool with slower flows and little bubble coalescence. When the power is off for 12.5 ms, bubbles have sufficient time with no Marangoni shear to escape; since the power off time is shorter, the reduction in pool size is small and bubbles are not captured. The results show that a 75% DC can achieve an optimal bubble minimisation for 20 Hz

frequency and mean power of 150 W, indicating that only a short laser off period can disrupt the Marangoni flow and reduce the flow velocity, enabling pore escape. This matches with minimal pore growth being observed at 50 - 500 Hz PW at 50% DC.

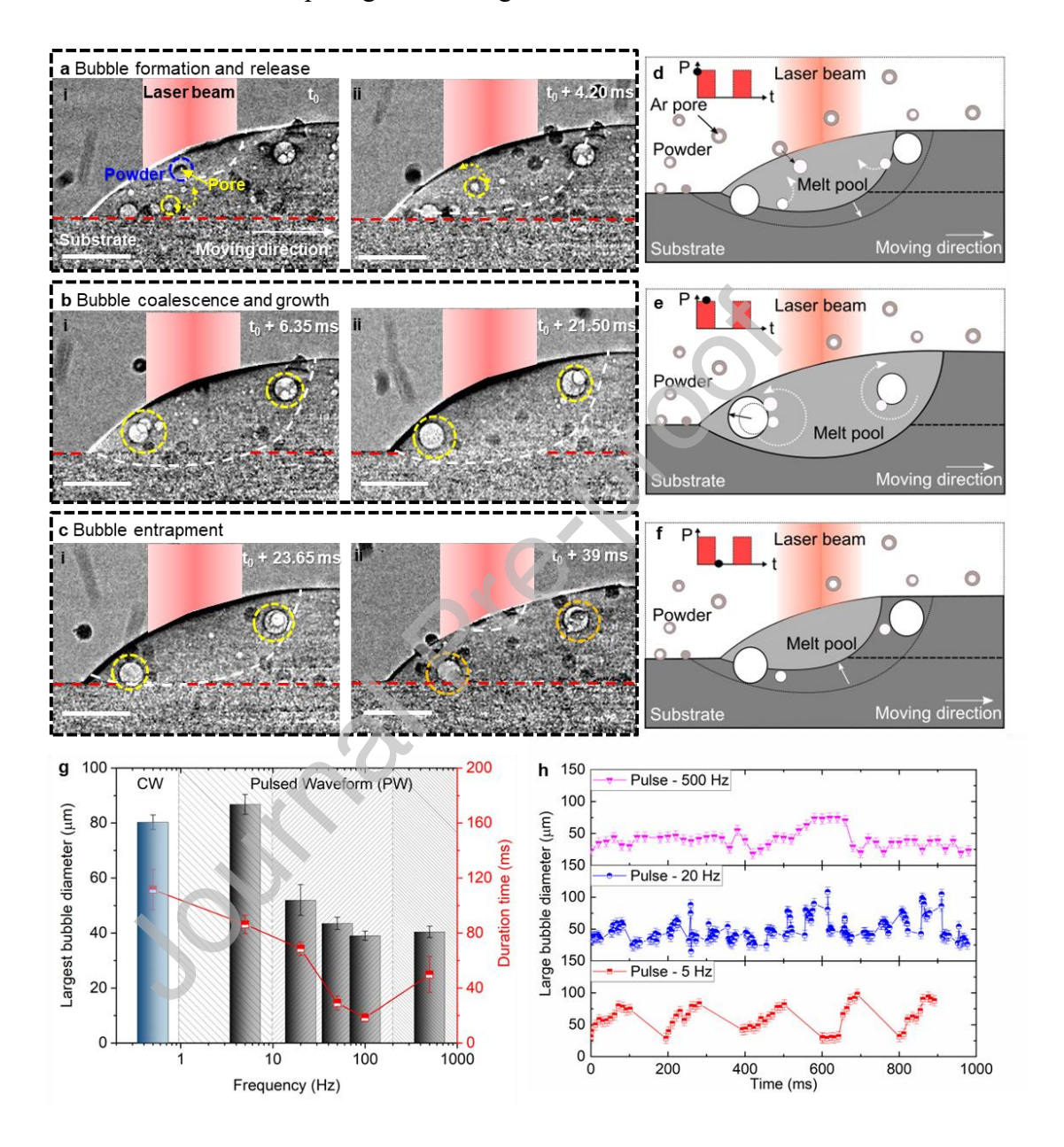


Fig. 3 Bubble behaviour and mechanisms during DED with pulsed waveform (PW) **mode laser.** (a) Radiographs of bubble formation and release at (a)-i $t = t_0$ and (a)-ii $t_0 + 4.2$ ms; blue dashed circles indicate pores in powder and previous build; bubble release and motion - yellow dashed circles and arrows. (b) Radiographs showing bubble coalescence and growth at (b)-i $t = t_0 + 6.35$ and (b)-ii $t_0 + 21.5$ ms. (c) Radiographs showing bubble

entrapment in the built track at (c)-i $t = t_0 + 23.65$ and (c)-ii $t_0 + 39$ ms at 20 Hz, entrapped pores indicated by orange dashed circles. (d to f) Corresponding schematic figures of (a to c). (g) The largest bubble diameter and duration time of bubble growth in a CW and PW mode at 5-500 Hz, and the error bar is the standard error of large bubble diameter and duration time in each cycle. (h) The large bubble diameter evolution with time in a PW mode at 5, 20, and 500 Hz, and diameter error bars are calculated as ± 2 pixels, equivalent to segmentation uncertainty. (The substrate traverse speed is 1 mm s⁻¹, mean and peak laser power is 150 and 300 W, PW mode and layer 1. See videos corresponding to (a to c), (g) and (h) in Movies S7-9. Scale bars: 300 µm).

Six-layer DED-AM builds were produced ex situ for the different conditions to compare with the *in situ* synchrotron results. The porosity in the final builds was investigated radiographically (Figs. S7-8) and tomographically (Fig. S9). Grain structure was investigated using EBSD, showing the modulated thermal field in 20 Hz SW helps refine the grain structure, producing finer and more equiaxed grains as compared to CW (Fig. S10). Examining the radiographs and tomographs (Figs. S7-9), large pores (ca. 170 um) are clearly visible in the CW mode sample at the end of a build track. In 5 Hz SW mode and 5, 20, 500 Hz PW there are a few medium sized pores (ca. 80 µm). However, at 20, 50, 100, 500 Hz SW, and 50 and 100 Hz PW, they are almost pore-lean and show ~99% and ~50% reduction in the max and mean pore volume compared to CW, and there are only a few small pores in a few cases (<50 μm). These results are consistent with the *in situ* X-ray imaging results shown in **Figs.** 2,3, confirming that our strategy of disrupting the Marangoni flow via modulating laser power at intermediate frequencies (20-500 Hz) minimises porosity. To further

confirm this hypothesis, we first track the bubble motion radiographically and then measure changes in the thermal field using infrared imaging.

3.4. Bubble motion and melt flow patterns

To confirm the mechanisms governing bubble behaviour for different laser modes, bubble motion was tracked in the radiographs, and tungsten (W) particles were added to reveal molten pool flow (see Methods). In Fig. 4a, bubble motion in CW mode includes bubble recirculation in the four Marangoni driven recirculating flow cells (Fig. 4e, front and back of the pool, and two in and out of the page [5]). In Fig. 2, when an argon pore in a feedstock particle is released into the pool it may recirculate several times, sometimes jumping between Marangoni flow cells (Fig. 4a), ending with either escape at the surface, coalescing into a large bubble, or becoming entrapped by the solidification front.

Bubble motion traces for CW and the different modes are shown in Fig. 4. In CW, and 5 Hz SW (Fig. 4a,b), the bubbles predominately recirculate at the front or back of the melt pool - the strong Marangoni driven flow cells constrain the bubbles enhancing coalescence and large bubble growth (see Fig. 2 and Movies S1 and S3). For 20 Hz SW, most bubbles first follow the surface Marangoni shear flow, then escape through the melt pool surface when the power is reduced (Fig. 4c), minimising bubble coalescence (Fig. 2). At the higher frequency of 500 Hz SW, the flow becomes similar to CW, but with bubbles recirculating in all four cells (rather than

predominately the front and back ones for CW), coalescing (Fig. 4d).

Tungsten tracer streaklines are shown in Fig. 4e for CW, and Fig. S11 for SW mode. In CW, the two recirculation flow cells at the front and rear of the melt pool are delineated (Fig. 4e and Fig. S8a), helping to constrain bubbles in the melt pool, enhancing coalescence. In 5 Hz SW mode, the W tracer tracks become quite complex due to the shrinking and growing pool size, as well as the changes in flow, as shown in Fig. S11b. At 20, 50 and 100 Hz SW the front/back recirculating flows remain, but the in/out of the page recirculation flow increases and then immediately becomes less strong (Fig. S11c-e), and the flow velocity at SW is also about 1/4 less than that for CW (Fig. S11h). This disrupted flow allows the bubbles to flow to the surface and escape. At 500 Hz (Fig. S11f), the stronger front/back recirculation flows are partially formed, allowing more coalescence.

Pulsed waveform mode bubble motion as a function of frequency (5-500 Hz PW) was investigated next (**Fig. 4f-h**). Similar to SW, at 5 Hz PW, many bubbles move laterally to coalesce and grow into large bubbles, with significant bubble recirculation and coalescence observed (Movies S3 and S8). At 20 Hz PW, although reduced, recirculation still occurs (unlike SW mode, compare **Fig. 4c** to **4g**) with significant bubble coalescence also still occurring. At 50 and 100 Hz PW, there is a minimum of pore coalescence (**Fig. 3g**); but at 500 Hz PW, the bubbles start to recirculate again (**Fig. 4h**), and like SW and CW modes, coalescence and maximum

bubble size both increase.

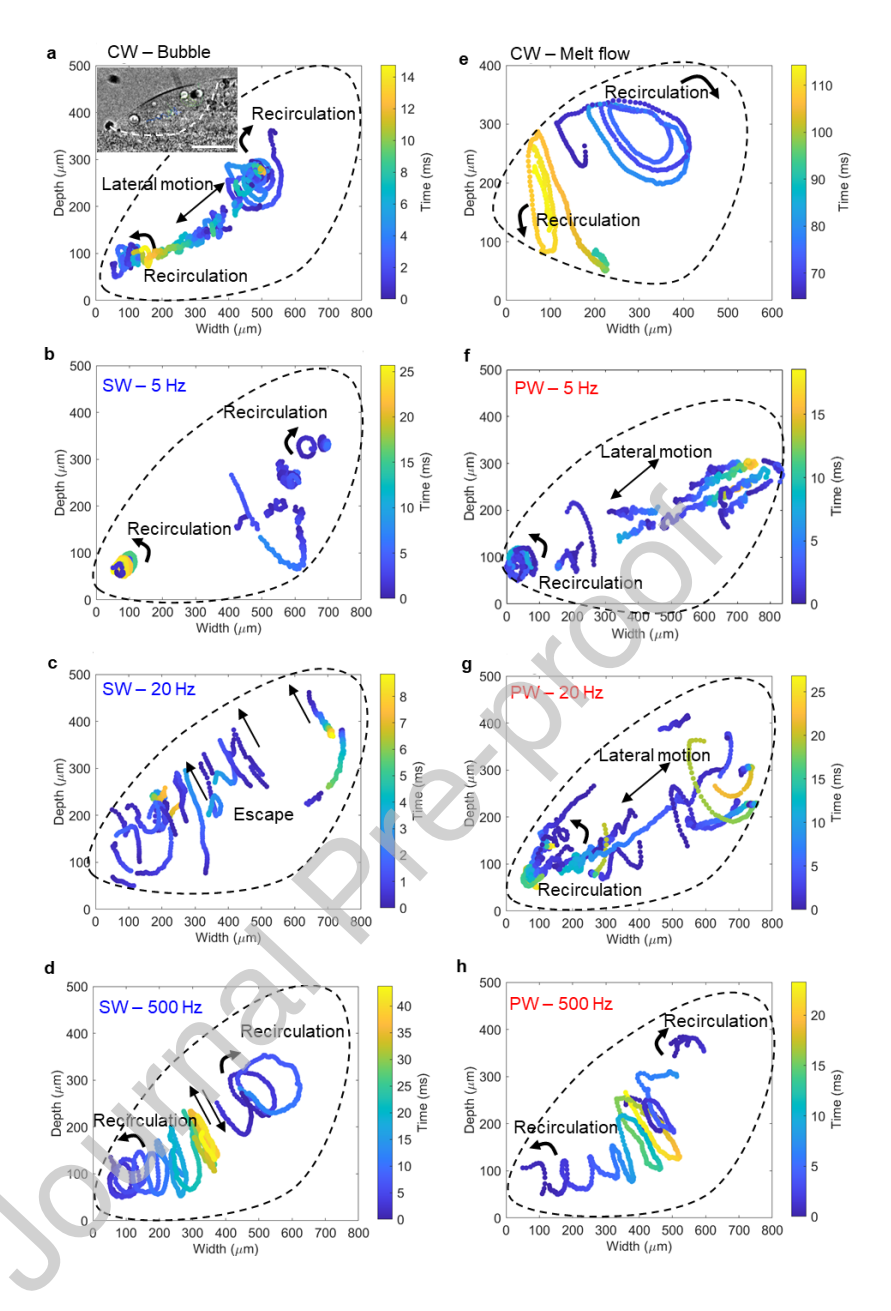


Fig. 4 Bubble motion and melt flow behaviour during DED in CW, SW and PW modes.

(a) Bubble motion path with time in CW mode and the inset showing its corresponding radiograph. (b) Bubble motion path with time for 5 Hz SW, (c) at 20 Hz SW and (d) at 500 Hz SW. (e) The W trace path with time indicating melt flow in CW mode. (f) Bubble motion for 5 Hz PW, (g) at 20 Hz PW and (h) at 500 Hz PW. (The mean laser power is 150 W, the peak laser power is 250 W in the SW mode and 300 W in the PW mode. The substrate traverse speed is 1 mm s⁻¹, layer 1. The dashed lines represent the melt pool boundary. See the

videos corresponding to (a to h) in Movies S1-4 and S7-9. Radiograph scale bar: 300 μm).

3.5. Thermal imaging and multiphysics modelling

Thermal imaging [14,32] and modelling [20,33,34] were performed to further test our hypothesis that laser modulation will alter the surface temperature gradient, impacting the Marangoni flow and hence bubble coalescence or escape. The results are shown for three exemplary cases in **Fig. 5**, CW, 20 Hz SW and 20 Hz PW at 150 W mean power. (Other frequencies modelled and IR imaged are given in **Figs. S12-21**).

Fig. 5a shows the predicted flow pattern for the CW case, and the IR surface temperature measurement is inset in Fig. 5a, and expanded in Fig. 5b; (note the IR image is taken at 40° from horizontal and transformed as compared to 0° for the model, see Methods). The centre of the pool is quite hot, and there is a strong gradient in temperature to the edge of the pool, quantified in Fig. 5c, showing an excellent correlation between prediction and IR measurement. This steep thermal gradient creates a strong surface tension gradient and hence a strong Marangoni force driven flow, creating the front, rear (and two sides) flow cells delineated by the bubble and W particle tracings in Fig. 4a,b. Fig. 5a,b show a strong hot spot where the laser hits with a high gradient to all edges of the pool. The measured values along the red dashed line (Fig. 5b) are plotted in Fig. 5c, together with the model predicted temperature profile. Both exhibit a similar peak temperature, although the IR

measured temperature gradient is slightly greater, which will lead to a slight under prediction of flow velocities. Both results confirm that a Marangoni force driven flow creates the high velocity recirculating flow cells at the front and back of the melt pool, and shear flow entraining the coalescing large bubbles.

The entrainment and bubble coalescence were also modelled (Fig. S21), illustrating how the strong Marangoni shear flow entrains the argon bubbles from the feedstock, enables coalescence, and then continues to entrain the resulting large bubbles in CW mode. Fig. 5d,e shows the model predictions for 20 Hz SW. At t_0 , maximum power (250 W), the flow and thermal field is similar to that of the CW case (compare Fig. 5d with 5a), although the flow is less strong as it has had to build up from the low flow at minimum power (50 W, Fig. 5e). The reduced flow spreads the heated metal more slowly, which coupled with a higher peak power (250 W), creates a higher peak temperature and gradient compared to CW (the model peak temperature of ~1970 K at 20 Hz SW compared to 1860 K at CW). At $t_0 + 25$ ms, when the power is at minimum, the thermal gradient is reduced (the model peak temperature of ~1970 K at t_0 compared to ~1670 K at $t_0 + 25$ ms), and hence the Marangoni flow decreases significantly, as quantified in Fig. 5f, correlating well with the IR measurements (Fig. 5d,e, and quantitatively in Fig. 5f). This predicted and measured reduction in Marangoni shear flow allows the bubbles to escape from the top surface, producing pore-lean DED builds, correlating well to the in situ synchrotron observations supporting our hypothesis.

The IR results for all SW and PW modes are given quantitatively for the peak temperature in Fig. S12 and as time series images in Fig. S13. Examining the model and IR results for 500 Hz SW laser power modulation in Fig. S18, the change in thermal profile between the maximum and minimum power levels is small, with the peak temperature altered by <100 °C compared to 300 °C for 20 Hz SW (Fig. 5d-f). This illustrates that 500 Hz SW is starting to act like CW, and hence bubbles are not escaping as easily, correlating directly with the *in situ* synchrotron observations.

To further confirm high frequencies matching CW, the model was run for 1000 Hz with bubbles, reproducing the same bubble behaviour as CW (Fig. S21d-f). The time scales in continuous and modulated modes at different frequencies are discussed in Supplementary Text and Table S1. The results show that the heat oscillation periods in the medium frequency of 20 to 500 Hz are comparable to the turnaround time of recirculation cells, and the heat diffusion length is in the similar scale to the cell diameter, which can affect the similar scale of recirculation cells to generate more effective bubble minimisation.

Fig. 5g,h shows the model predictions when a 20 Hz PW modulation is applied. At t_0 , when the power is at maximum, the flow and thermal field is similar to CW (compare **Fig. 5d** with **5a**). Like SW results, the flow is less strong than CW, as it has had to build up from almost no flow at minimum power (**Fig. 5h**). Again, the higher peak power and reduced flow predicts the peak temperature at the centre to go

significantly higher than CW, as confirmed by the IR measurements in **Fig. 5i**. This increased peak temperature and larger pool allows pore coalescence, making PW less effective than SW for pore escape, correlating well to the *in situ* synchrotron observations (**Figs 1, 3, and 4**).

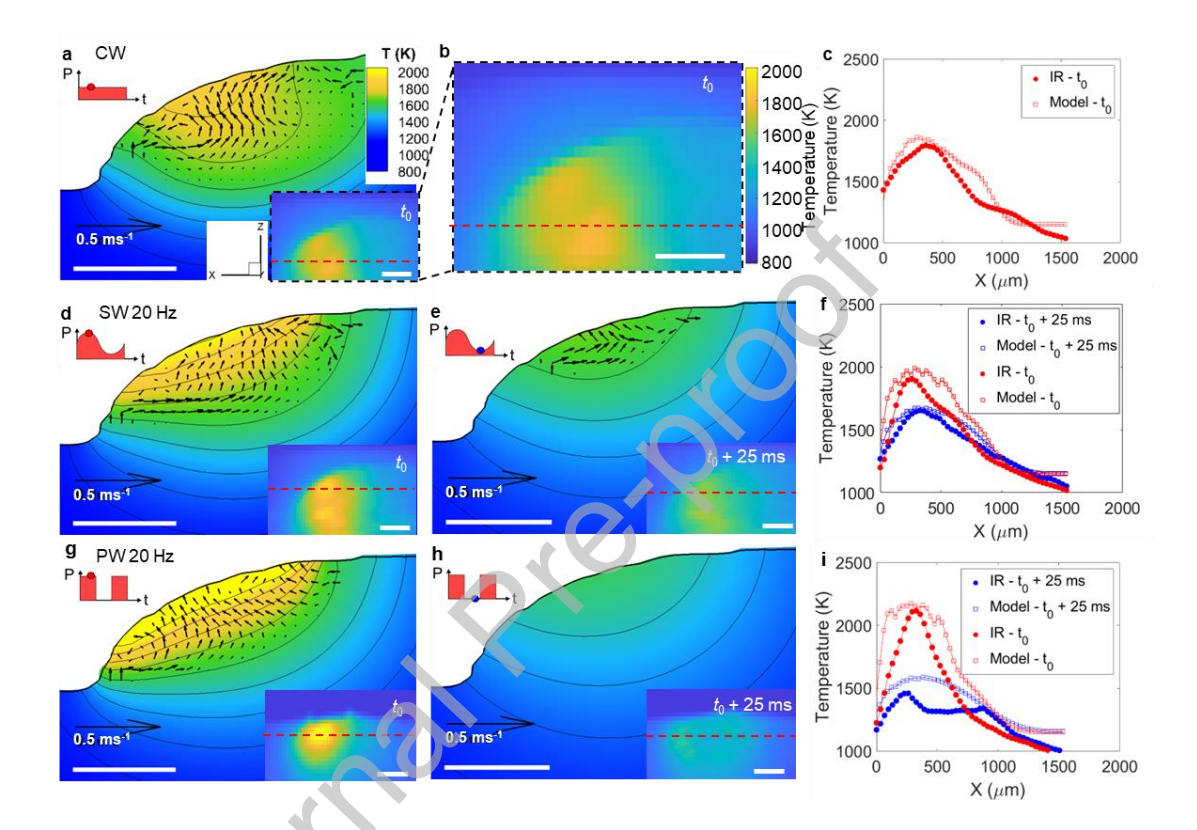


Fig. 5 Multiphysics modelling and corresponding IR imaging results during DED in CW, SW, and PW modes. (a) Simulation temperature and velocity fields for CW mode and inset showing the corresponding IR measured temperature field. (b) Enlarged image showing the temperature field measured by IR imaging. (c) Corresponding temperature profiles of IR imaging and modelling in the CW mode. (d) Simulation temperature and velocity fields for 20 Hz SW, and predictions (inset IR images) at t_0 , and (e) at $t_0 + 25$ ms. (f) 20 Hz SW IR and modelling temperature profiles at t_0 and $t_0 + 25$ ms. (g) Simulation temperature and velocity fields for 20 Hz PW, and inset IR images, at t_0 , and (h) at $t_0 + 25$ ms. (i) Corresponding IR and modelling temperature profiles for 20 Hz PW at t_0 and $t_0 + 25$ ms. (Scale bars 300 μ m. See videos corresponding to (a) and (b), (d) and (e), (g) and (h) in Movies S10-11, S12-14 and

4. Conclusions

In summary, our correlative *in situ* synchrotron and IR imaging observations, coupled with high fidelity modelling revealed the large pore formation mechanisms (coalescence of argon bubbles from the feedstock) during DED. These insights enabled us to develop a novel method for creating pore-lean AM builds – through applying low-medium frequency (20-500 Hz) laser modulation. We comprehensively investigate bubble behaviour in sine wave (SW) and pulsed wave (PW) modulated laser power modes, with varying frequency and amplitudes, whilst using continuous wave (CW) mode as the benchmark. We found that the bubble coalescence that creates large bubbles (>50 μm) can be significantly minimised using SW and PW modes with medium range frequencies from 20 to 500 Hz, particularly in SW mode.

Bubble coalescence is minimised through disruption of the Marangoni force driven surface shear flow, as the flow keeps the coalescing bubbles from escaping at the surface. This mechanism is activated by short reductions in laser power, reducing the surface temperature and hence the thermal gradient, which in turn reduces the gradient in surface energy, slowing the Marangoni flow and enabling pore release at the surface. The bubble control mechanisms discovered here provide a way to achieve defect-lean DED additive manufacturing.

Data availability

All key data are available in the main text or the supplementary materials, the radiographs are available upon reasonable request from the corresponding authors.

CRediT authorship contribution statement

Kai Zhang: Conceptualization, Data curation, Formal analysis, Investigation, Methodology, Software, Validation, Visualization, Writing - original draft, Writing - review and editing. Shishira Bhagavath: Data curation, Investigation. Sebastian Marussi: Methodology, Investigation. Alexander Rack: Methodology, Data curation, Investigation. Robert Atwood: Methodology, Data curation, Investigation. Martyn A. Jones: Investigation. Chu Lun Alex Leung: Investigation, Writing - review and editing. Chinnapat Panwisawas: Investigation. Junji Shinjo: Software, Investigation, Writing - review and editing. Peter D. Lee: Conceptualization, Funding acquisition, Investigation, Methodology, Writing - review and editing.

Declaration of competing interests

K.Z., M.A.J. and P.D.L. declare a filed patent application (GB2408301.6) related to this work. The author is an Editorial Board Member/Editor-in-Chief/Associate Editor/Guest Editor for this journal and was not involved in the editorial review or the decision to publish this article. All other authors declare no competing interests.

Acknowledgements

We acknowledge the Research Complex at Harwell for use of the facilities, Diamond Light Source (DLS) for providing beam time at beamline I12: JEEP (MG31855), and the European Synchrotron Radiation Facility for providing beam time at beamline ID19 (MA5497). We also thank all the beamline staff who helped at both facilities, and all the groups' members who helped, especially Imogen Cowley, Xianqiang Fan, Li Wei, Harry Chapman, David Rees, Yunhui Chen, Maureen Fitzpatrick. Funding: This research is financially supported by UK-EPSRC via MAPP: Future Manufacturing Hub in Manufacture using Advanced Powder Processes and other grants (EP/P006566/1, EP/W006774/1, EP/W031167/1, and EP/V061798/1), Rolls-Royce plc. via the Aerospace Technology Institute program REINSTATE (contract 51689), and the Royal Academy of Engineering (CiET1819/10) (P.D.L.). This work is partially supported by Next Generation TATARA Project sponsored by the Government of Japan and Shimane Prefecture (J.S.); Innovation Fellowship funded by Engineering and Physical Science Research Council (EPSRC), UK Research and Innovation, under the grant number EP/S000828/2 (C.P.); EPSRC EP/W037483/1 and IPG Photonics/ Royal Academy of Engineering Senior Research Fellowship in SEARCH (RCSRF2324-18-71) (C.L.A.L.); EPSRC-IAA project grant (K.Z.).

Appendix A. Supplementary material

Supplementary Information to this article can be found in the Supplementary Material document.

References

- [1] D. Gu, X. Shi, R. Poprawe, D.L. Bourell, R. Setchi, J. Zhu, Material-structure-performance integrated laser-metal additive manufacturing, Science (80-.). 372 (2021) eabg1487. https://doi.org/10.1126/science.abg1487.
- Y. Chen, S.J. Clark, D.M. Collins, S. Marussi, S.A. Hunt, D.M. Fenech, T. Connolley, R.C. Atwood, O. V. Magdysyuk, G.J. Baxter, M.A. Jones, C.L.A. Leung, P.D. Lee, Correlative synchrotron X-ray imaging and diffraction of directed energy deposition additive manufacturing, Acta Mater. 209 (2021). https://doi.org/10.1016/j.actamat.2021.116777.
- [3] Z. Yang, S. Wang, L. Zhu, J. Ning, B. Xin, Y. Dun, W. Yan, Manipulating molten pool dynamics during metal 3D printing by ultrasound, Appl. Phys. Rev. 9 (2022) 21416. https://doi.org/10.1063/5.0082461.
- [4] D. Svetlizky, M. Das, B. Zheng, A.L. Vyatskikh, S. Bose, A. Bandyopadhyay, J.M. Schoenung, E.J. Lavernia, N. Eliaz, Directed energy deposition (DED) additive manufacturing: Physical characteristics, defects, challenges and applications, Mater. Today 49 (2021) 271–295. https://doi.org/10.1016/j.mattod.2021.03.020.
- [5] K. Zhang, Y. Chen, S. Marussi, X. Fan, M. Fitzpatrick, S. Bhagavath, M. Majkut, B. Lukic, K. Jakata, A. Rack, M.A. Jones, J. Shinjo, C. Panwisawas, C.L.A. Leung, P.D. Lee, Pore evolution mechanisms during directed energy deposition additive manufacturing, Nat. Commun. 15 (2024) 1715. https://doi.org/10.1038/s41467-024-45913-9.
- [6] D. Zhang, D. Qiu, M.A. Gibson, Y. Zheng, H.L. Fraser, D.H. StJohn, M.A. Easton, Additive manufacturing of ultrafine-grained high-strength titanium alloys, Nature 576 (2019) 91–95. https://doi.org/10.1038/s41586-019-1783-1.
- [7] J.H. Martin, B.D. Yahata, J.M. Hundley, J.A. Mayer, T.A. Schaedler, T.M. Pollock, 3D printing of high-strength aluminium alloys, Nature 549 (2017)

- 365–369. https://doi.org/10.1038/nature23894.
- [8] S. Wang, J. Ning, L. Zhu, Z. Yang, W. Yan, Y. Dun, P. Xue, P. Xu, S. Bose, A. Bandyopadhyay, Role of porosity defects in metal 3D printing: Formation mechanisms, impacts on properties and mitigation strategies, Mater. Today 59 (2022) 133–160. https://doi.org/https://doi.org/10.1016/j.mattod.2022.08.014.
- [9] D.D. Gu, W. Meiners, K. Wissenbach, R. Poprawe, Laser additive manufacturing of metallic components: Materials, processes and mechanisms, Int. Mater. Rev. 57 (2012) 133–164. https://doi.org/10.1179/1743280411Y.0000000014.
- [10] R. Biswal, A.K. Syed, X. Zhang, Assessment of the effect of isolated porosity defects on the fatigue performance of additive manufactured titanium alloy, Addit. Manuf. 23 (2018) 433–442. https://doi.org/10.1016/j.addma.2018.08.024.
- [11] P.D. Lee, J.D. Hunt, Measuring the nucleation of hydrogen porosity during the solidification of aluminium-copper alloys, Scr. Mater. 36 (1997) 399–404. https://doi.org/10.1016/S1359-6462(96)00411-3.
- [12] Y. Huang, T.G. Fleming, S.J. Clark, S. Marussi, K. Fezzaa, J. Thiyagalingam, C.L.A. Leung, P.D. Lee, Keyhole fluctuation and pore formation mechanisms during laser powder bed fusion additive manufacturing, Nat. Commun. 13 (2022) 1170. https://doi.org/10.1038/s41467-022-28694-x.
- [13] C. Zhao, N.D. Parab, X. Li, K. Fezzaa, W. Tan, A.D. Rollett, T. Sun, Critical instability at moving keyhole tip generates porosity in laser melting, Science (80-.). 370 (2020) 1080–1086. https://doi.org/10.1126/science.abd1587.
- [14] Z. Ren, L. Gao, S.J. Clark, K. Fezzaa, P. Shevchenko, A. Choi, W. Everhart, A.D. Rollett, L. Chen, T. Sun, Machine learning—aided real-time detection of keyhole pore generation in laser powder bed fusion, Science (80-.). 379 (2023) 89–94. https://doi.org/10.1126/science.add4667.
- [15] S. Webster, N. Moser, K. Fezzaa, T. Sun, K. Ehmann, E. Garboczi, J. Cao,

- Pore formation driven by particle impact in laser powder-blown directed energy deposition, PNAS Nexus 2 (2023) 1–9. https://doi.org/10.1093/pnasnexus/pgad178.
- [16] S.M.H. Hojjatzadeh, N.D. Parab, W. Yan, Q. Guo, L. Xiong, C. Zhao, M. Qu, L.I. Escano, X. Xiao, K. Fezzaa, W. Everhart, T. Sun, L. Chen, Pore elimination mechanisms during 3D printing of metals, Nat. Commun. 10 (2019) 1–8. https://doi.org/10.1038/s41467-019-10973-9.
- [17] S.J. Wolff, H. Wang, B. Gould, N. Parab, Z. Wu, C. Zhao, A. Greco, T. Sun, In situ X-ray imaging of pore formation mechanisms and dynamics in laser powder-blown directed energy deposition additive manufacturing, Int. J. Mach. Tools Manuf. 166 (2021). https://doi.org/10.1016/j.ijmachtools.2021.103743.
- [18] R. Cunningham, C. Zhao, N. Parab, C. Kantzos, J. Pauza, K. Fezzaa, T. Sun, A.D. Rollett, Keyhole threshold and morphology in laser melting revealed by ultrahigh-speed x-ray imaging, Science (80-.). 363 (2019) 849–852. https://doi.org/10.1126/science.aav4687.
- [19] Q. Guo, C. Zhao, M. Qu, L. Xiong, S.M.H. Hojjatzadeh, L.I. Escano, N.D. Parab, K. Fezzaa, T. Sun, L. Chen, In-situ full-field mapping of melt flow dynamics in laser metal additive manufacturing, Addit. Manuf. 31 (2020) 100939. https://doi.org/10.1016/j.addma.2019.100939.
- [20] S.A. Khairallah, A.A. Martin, J.R.I. Lee, G. Guss, N.P. Calta, J.A. Hammons, M.H. Nielsen, K. Chaput, E. Schwalbach, M.N. Shah, M.G. Chapman, T.M. Willey, A.M. Rubenchik, A.T. Anderson, Y. Morris Wang, M.J. Matthews, W.E. King, Controlling interdependent meso-nanosecond dynamics and defect generation in metal 3D printing, Science (80-.). 368 (2020) 660–665. https://doi.org/10.1126/science.aay7830.
- [21] C.L.A. Leung, S. Marussi, R.C. Atwood, M. Towrie, P.J. Withers, P.D. Lee, In situ X-ray imaging of defect and molten pool dynamics in laser additive manufacturing, Nat. Commun. 9 (2018) 1–9. https://doi.org/10.1038/s41467-

- 018-03734-7.
- [22] S. Hocine, H. Van Swygenhoven, S. Van Petegem, C.S.T. Chang, T. Maimaitiyili, G. Tinti, D. Ferreira Sanchez, D. Grolimund, N. Casati, Operando X-ray diffraction during laser 3D printing, Mater. Today 34 (2020) 30–40. https://doi.org/10.1016/j.mattod.2019.10.001.
- [23] C.L.A. Leung, S. Marussi, M. Towrie, R.C. Atwood, P.J. Withers, P.D. Lee, The effect of powder oxidation on defect formation in laser additive manufacturing, Acta Mater. 166 (2019) 294–305. https://doi.org/10.1016/j.actamat.2018.12.027.
- [24] G. Dai, Z. Sun, Y. Li, J. Jain, A. Bhowmik, J. Shinjo, J. Lu, C. Panwisawas, Grain refinement and columnar-to-equiaxed transition of Ti6Al4V during additive manufacturing via different laser oscillations, Int. J. Mach. Tools Manuf. 189 (2023) 104031. https://doi.org/10.1016/j.ijmachtools.2023.104031.
- [25] Y. Hu, S. Wu, Y. Guo, Z. Shen, A.M. Korsunsky, Y. Yu, X. Zhang, Y. Fu, Z. Che, T. Xiao, S. Lozano-perez, Q. Yuan, X. Zhong, X. Zeng, G. Kang, P.J. Withers, Inhibiting weld cracking in high-strength aluminium alloys, Nat. Commun. 13 (2022) 5816. https://doi.org/10.1038/s41467-022-33188-x.
- [26] S.M.H. Hojjatzadeh, Q. Guo, N.D. Parab, M. Qu, L.I. Escano, K. Fezzaa, W. Everhart, T. Sun, L. Chen, In-situ characterization of pore formation dynamics in pulsed wave laser powder bed fusion, Materials (Basel). 14 (2021) 1–11. https://doi.org/10.3390/ma14112936.
- [27] S. Gao, W. Ji, Q. Zhu, A. Jarlöv, X. Shen, X. Bai, C. Zhu, Y.Z. Lek, Z. Xiao, K. Zhou, Pulsed-wave laser additive manufacturing of CrCoNi medium-entropy alloys with high strength and ductility, Mater. Today 81 (2024) 36–46. https://doi.org/10.1016/j.mattod.2024.10.004.
- [28] S. Liao, S. Webster, D. Huang, R. Council, K. Ehmann, J. Cao, Simulation-guided variable laser power design for melt pool depth control in directed energy deposition, Addit. Manuf. 56 (2022) 102912.

- https://doi.org/10.1016/j.addma.2022.102912.
- [29] J.Y. Tinevez, N. Perry, J. Schindelin, G.M. Hoopes, G.D. Reynolds, E. Laplantine, S.Y. Bednarek, S.L. Shorte, K.W. Eliceiri, TrackMate: An open and extensible platform for single-particle tracking, Methods 115 (2017) 80–90. https://doi.org/10.1016/j.ymeth.2016.09.016.
- [30] J. Shinjo, C. Panwisawas, Chemical species mixing during direct energy deposition of bimetallic systems using titanium and dissimilar refractory metals for repair and biomedical applications, Addit. Manuf. 51 (2022) 102654. https://doi.org/10.1016/j.addma.2022.102654.
- [31] C. Panwisawas, Y. Gong, Y. Tony, R.C. Reed, J. Shinjo, Additive manufacturability of superalloys: Process-induced porosity, cooling rate and metal vapour, Addit. Manuf. 47 (2021) 102339. https://doi.org/10.1016/j.addma.2021.102339.
- [32] P.A. Hooper, Melt pool temperature and cooling rates in laser powder bed fusion, Addit. Manuf. 22 (2018) 548–559. https://doi.org/10.1016/j.addma.2018.05.032.
- [33] L. Wang, Q. Guo, L. Chen, W. Yan, In-situ experimental and high-fidelity modeling tools to advance understanding of metal additive manufacturing, Int. J. Mach. Tools Manuf. 193 (2023) 104077. https://doi.org/https://doi.org/10.1016/j.ijmachtools.2023.104077.
- [34] A.A. Martin, N.P. Calta, S.A. Khairallah, J. Wang, P.J. Depond, A.Y. Fong, V. Thampy, G.M. Guss, A.M. Kiss, K.H. Stone, C.J. Tassone, J. Nelson Weker, M.F. Toney, T. van Buuren, M.J. Matthews, Dynamics of pore formation during laser powder bed fusion additive manufacturing, Nat. Commun. 10 (2019) 1–10. https://doi.org/10.1038/s41467-019-10009-2.

Graphical Abstract

